Cross-sectional characterization of the exhaust of a Pulsed Plasma Thruster

IEPC-2024-610

Presented at the 38th International Electric Propulsion Conference, Toulouse, France
June 23-28, 2024

Scherezade Barquero,* Jaume Navarro-Cavallé and Mario Merino.
Department of Aerospace Engineering, Universidad Carlos III de Madrid, Leganés, Spain

Abstract: The time-resolved expansion of the exhaust of a small ablative pulsed plasma thruster (PPT) prototype has been experimentally characterized by means of a novel diagnostic system consisting of a grid of Langmuir probes working in the ion saturation regime. The 2D ion current distribution is reconstructed from the probe data using a variable separation algorithm. The plume of the PPT, operated at 1000 V of discharge voltage and 6 μF, exhibits three separate ion groups, with the second one carrying the major part of the ion current. The plasma beam is single-peaked and less spread in the x direction (i.e. the cathode-to-anode direction), while it shows two peaks in the y direction. Asymmetries are present in the exhaust, showing some deviation of the current towards the anode electrode and one of the lateral sides of the channel. Beyond their relevance on the characterization of the time-dependent exhaust divergence angle, the thruster performance and their interest for spacecraft/plume interaction analyses, these results constitute an additional step towards a clearer understanding of the discharge physics in PPTs.

I. Introduction

Ablative pulsed plasma thrusters (APPT)[1–3] are electromagnetic space propulsion systems that consist of a pair of electrodes (cathode-anode) shaping a channel-like configuration, connected to an energy storage unit, typically a capacitor bank. On one end of the channel, solid propellant, normally PTFE, is placed between the electrodes. Once the capacitor bank is charged up to a sufficiently large voltage V_0, a discharge is triggered by means of a spark plug over the surface of the propellant, whereby a fraction of it is ablated and ionized by the resulting electric current.[4–6] This discharge current also generates a self-induced magnetic field that causes a Lorentz force, which accelerates the generated plasma downstream and away from the device, generating thrust. Since APPTs operate in pulsed mode, the discharge energy per pulse can be controlled independently and irrespectively of the available input power, by modifying the pulse rate. This, combined with their potential to be compact and simplicity, makes APPTs ideal for microsatellites (with $<$ 30 W being typical).[3,7] This contrasts with continuous-operation plasma thrusters, such as Hall thrusters, which are notoriously difficult to scale down to low powers.[8] However, the discharge process of APPTs is complex and involves multiple phenomena, including breakdown, propellant ablation and dissociation, formation of the ionization layer and plasma generation, acceleration, and, finally, exhaust ejection and expansion.[9] The simultaneity and spatial coincidence of these mechanisms hinder their separated analysis.[10] Additional phenomena such as late-time ablation,[2,6,11–14] secondary breakdowns,[9,15–19] and particulate emission[20,21] can take place in the discharge. Furthermore, for the usual solid propellants used, the resulting plasma may be composed of multiple chemical species at different charge states.[12,13,15,19,22]

Beyond serving to characterize the performances of specific prototypes and the spacecraft/plume interaction, laboratory measurements of the plasma exhaust are essential to supplement the models and to help in the understanding of APPTs. Since the 60s, manifold research teams have characterized APPTs at various energy levels,[3,6,12–16,19,20,22–36] nevertheless, studies on plume expansion are scarce. For an 80–100 J/2.5–2.8 kV PTFE parallel-rail APPT, Antropov et al.[12] reported the electron density cross distribution

*mbalsera@ing.uc3m.es.

within the plane parallel to the electrode surface, along one of the channel sides, at different times of interest. Local measurements were carried out by means of single Langmuir probes. A plasma jet divergence angle (i.e., beam width) between $\sim$ 44°–80°, respectively for the maximal density level and for the 10%. The measured data only covers one side of the plane, at which the density maximum is displaced with respect to the thruster longitudinal axis. The PTFE parallel-rail LES 8/9 APPT plume cross distribution was also investigated.[23,37] Operating it at 20 J/1–2 kV, Myers et al.,[23] carried out contamination diagnostics, by using a large number of collimated quartz contamination sensors, and planar and single Langmuir probes, in both the near- and far-field regions. Published data is not time-resolved. No measurable deposition in the backflow region was found. Forward measurements revealed single-peak profiles with sensitivity to channel configuration, as the inherent asymmetry resulting from using a planar electrodes. I.e., the ion current profile is significantly flatter parallel to the electrodes than perpendicular, respectively decreasing by $\sim$ 25% and by a factor of $\sim$ 3.5 with 40° of the thruster axis. In both planes, current density drops by over a factor of 25 within 75° of the thruster longitudinal axis. Only minor effects were measurable at $50, 60°$ at the near and far field correspondingly. Vondra et al.[38] explored the exhaust cross profile within the parallel-to-electrode plane of the PTFE APPT LES 6 (1.85 J/1360 V). By means of a Faraday cup, they reported a full beam width of about 36°, single-peak, and slightly deviated towards one of the sides. Time resolved data is neither provided. More recent, Jakubczak et al.[39] have reported the retarding-potential-analyzer measurements carried out within the two cross planes of a 1 J/1000 V parallel-rail PTFE APPT. The time-resolved data exhibit significant axial asymmetry, i.e., ion charge density profile is notably wider along the plane parallel to the electrodes than towards the perpendicular one. The cross profiles are single-peak in both cases, whose maximum almost aligns with the thruster axis. Ion collection is still noticeable at 85° from the thruster axis, but significant current density is confined within ±45° from the channel centerline along the obstructed plane and ±60° along the unobstructed one.

It is also possible to obtain a first estimate of the exhaust plume divergence rate from the decrease in peak current value from one time-of-flight probe to the next, placed along the thruster longitudinal axis. This was done in one of our previous works[40] by using Langmuir probes. However, simply correlating features among probe signals neglecting the two following aspects yield a lack of accuracy. First, the fact that the exhaust likely consists of more than one ion group (each one of them potentially originating at a different time, and with different charge/mass ratios, velocities, densities, thermal spreads and divergence rates). Second, the ion current density of each ion group decreases downstream not only due to the divergence, but due to the axial thermal spread. To overcome these limitations, a method to reconstruct the parameters of the ion populations from the entire time series data, by establishing a model of their expansion, was proposed.[19] The fitted results of that work reveal that the model offers an accurate description o the exhaust with the superposition of only three ion groups. Additionally, these groups are characterized at different operational conditions and trends, discussed. Though, the thermal spread and the divergence parameter exhibit less clear trends. Among other aspects, placing additional probes, on-axis and off-axis, may improve the fit conditioning, as they would provide additional data on the plume, by reducing uncertainty on some of the parameters.

In order to shed more light on these unknowns, a novel diagnostic technique to easy access the time-varying current density distribution along the PPT plume cross section is presented in this work. This technique is then used to characterize a small APPT breadboard model, named PμLSA (PULSed Ablative PPT for micro/μ-propulsion) at its nominal operational point (1000 V, 6 μF, 3 J). To this aim, a fast-sampled Langmuir probe grid working in the ion saturation regime is developed to 2D scan the plume cross section by measuring the line integral of the current distribution. A simple algorithm to resolve the inverse reconstruction problem by variable separation is proposed.

The rest of the document is structured as follows. Section II presents the APPT prototype and the experimental setup to scan the plume cross section. Section III describes reconstruction algorithm. Section IV collects and discuss the results. Finally, conclusions and next steps are summarized in Section V.

II. Experimental setup

A. PμLSA prototype

A low-power, breech-fed, parallel-rail, rectangular-electrodes PTFE APPT breadboard model, named PμLSA (Figure 1), is the object of experimental study in this work. The first ignition and the architecture of the thruster has been reported,[40] and some plasma plume properties have been also analyzed.[19] In this work, a

different model of capacitors is used. The thruster nominal operational point is set at 1000 V of discharge voltage V_0 and 6 μF of capacitance C, resulting a storage energy of 3 J.

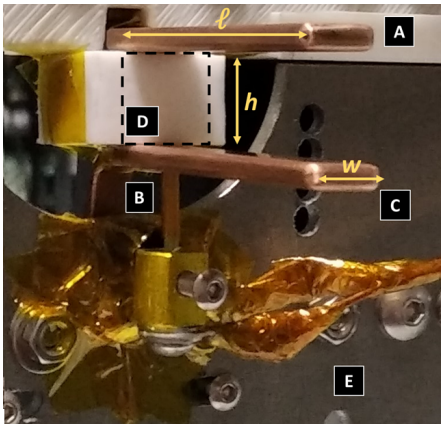

Figure 1: **Discharge channel of the PμLSA APPT prototype.** "C" is the cathode electrode,"A", the anode electrode, "B", the spark plug, "D", the exposed propellant surface (PTFE), and "E", the mounting structure. Dimensions l, h and w stand for the channel length, height and width, respectively.

The reference system used (see figure 3(a)) sets the z axis pointing away, from the point of view of the thruster, following the plume. The x axis is parallel to the electric field positive with it. The y axis completes the right-handed trihedron, parallel to the self-induced magnetic field and positive with it. Note that in this work, contrary to typical x, y plot arrangements, the x axis is vertical and the y axis, horizontal.

The thruster is operated inside Hedron, a $50 \times 50 \times 50$ cm cubic vacuum chamber available at the EP2 laboratory at Universidad Carlos III de Madrid (UC3M). MHV high voltage feedthroughs are used for the charging lines of the main and sparkplug capacitor banks. Hedron is equipped with a mechanical vacuum pump, Edwards nXDS Scroll pump, 10 m^3/h; and, a turbomolecular pump Edwards next400, 400 L/s N_2. The ultimate pressure reached is in the 10^{-6} mbar range. At each firing, the pressure rises to values below $2 \cdot 10^{-5}$ mbar, and is able to go back to the ultimate pressure within a few seconds.

Teledyne LeCroy high voltage passive probes were used for voltage monitoring of the main discharge capacitor bank. This signal is used as trigger for the diagnostics data acquisition by using the eight-analog-channel Yokogawa DLM5000 oscilloscope. It is used for data acquisition from all the probes synchronously, voltage and plasma ones described in the following section, Section B. The oscilloscope sampling frequency is set at 100 MHz.

B. Plume cross section scanner

A new diagnostic system has been developed to measure the 2D time-varying cross section of the transient plume of a PPT, displayed in figure 2. This system takes advantage of the principle of operation of Langmuir type probes, working in the ion saturation regime, when these are distributed in a 2D matrix.

The proposed system consists of an aluminum frame that holds a series of 8 parallel and independent wire probes distributed every 2 cm within the xy plane. The probes can be aligned with the x and y axes respectively. The same reference axes described in Section A are used for the plasma probe grid. The probes are naked tungsten filaments with 0.502 mm diameter, spanning a measurement length of 19.2 cm each. At one probe extreme, fitted PTFE tubes are used to electrically separate the probes from the frame. At the other probe side, BNCs are used to wire the probes and to hold them to the frame; ceramic paste insulates the connector and its connection point with the probe from the plume. The frame is grounded in this experiment, but keeping it floating has no effect on the measurements. Coaxial wires, to minimize noise, and BNC feedthroughs are used to bring the signals out.

These probes are negatively biased to operate within the ion saturation current regime. It has been checked that for a bias about -120 V, the current is well saturated at any explored location. The current to each probe can be measured simultaneously through a resistor bank by means of voltage probes and the oscilloscope. The probe electrical circuit used in this experiment is different to the one of our cited previous

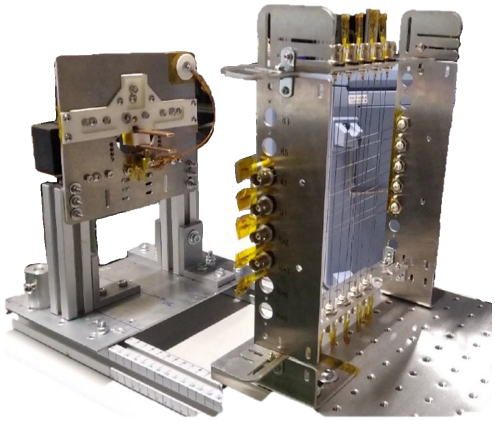

Figure 2: **Photograph of the experimental setup, showing the thruster and the probe array to scan the plume cross section positioned downstream.**

work,[19] including the area enclosed by the circuit. This aspect may involve slight variations in the frequency resolution of the collected signal.

As shown in figure 3(a), the probe plane has been set at an axial distance $z_{grid} = 15.3$ cm from the PTFE propellant surface. To cover a plume cross section as large as possible, the plume has been divided into 4 positionings s, and the probe array has been placed on each of them. Additionally, scanning the plume cross section by different positionings allows a more accurate local description. Distributed as in figure 3(a),(b), these positionings are named: right-bottom (RB), left-bottom (LB), right-top (RT), left-top (LT). 2.5 cm of overlap exists between positionings along the probe direction to separate the framefrom the region of interest. To validate the measurements and rule out any impact of the probe array location on the measurements, the $x = 0$ and $y = 0$ locations are measured and compared from each one of the positionings. Hence, double measurements at the four $i, j = 8$ locations exist. Hence, 32 different horizontal measurements along the x axis can be collected, with 8 of them distributed within each positioning, and another 32 vertical ones along the y axis. These correspond to 30 different horizontal locations, 30 vertical ones respectively, involving between the two datasets 4 double locations at the central "crosshair" (at $x = 0$ and $y = 0$), 2 each.

The maximum number of horizontal or vertical probes that can be used at a time is 6. The perturbation on the bias is also monitored simultaneously to them. Ideally, in total, the experimental campaign can be carried out in 16 separate tests, each requiring a repositioning of the frame or the connection of a different set of probes, to fully characterize the cross section. Best case, it could be reduced to 8 for only repositioning the frame in case of having the chance to measure the entire positioning at once. Typically, ≥ 50 measurements were considered for each test to achieve statistical significance of the mean signals to be analyzed in the rest of this work. It was noted that, while an analogous characterization of the plume is possible with a single probe with a similar resolution, by requiring 50 valid measurements on each measurement point, that procedure would require at least a total of 3000 firings, that is 7.5 times more than in the best case of the present approach. The main technical difficulties of the present experimental campaign involved discharge phenomena between the probes and the PPT exhaust, especially at probe locations where plasma density is higher. These affected measurements were discarded, becoming comparable in certain cases to the size of the useful sample of firings. This phenomenon limited the size to the valid firing sample to < 30 on multiple horizontal locations, different to $x = 0$, along RT and L positionings. As well, it led H_{RB6},H_{RB4},H_{RB9} to be replaced by the averages of the neighboring locations. While there is room for improvement in future work, the previous decisions have been validated as representative.

To reduce high-frequency noise in some of the signals, considered irrelevant for the present work, a low pass filter at 5 MHz has been subsequently applied to the measurements presented in the next sections.

III. Cross-section reconstruction algorithm

The probe grid diagnostic system allows to reconstruct the ion current density distribution of the PPT plume cross section as a function of time, $j(x, y, t)$. The algorithm used is described next.

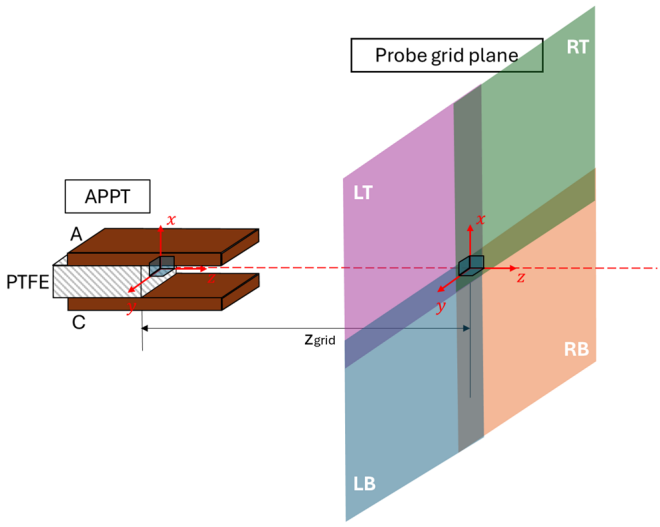

(a) Sketch of the experiment setup. "A" refers to anode, and "C" to cathode. The plume probe array measuring plane is at $z_{grid} = 15.3$ cm from the propellant surface. Right-bottom (RB), left-bottom (LB), right-top (RT) and left-top (LT) are the different positionings for the probe array used.

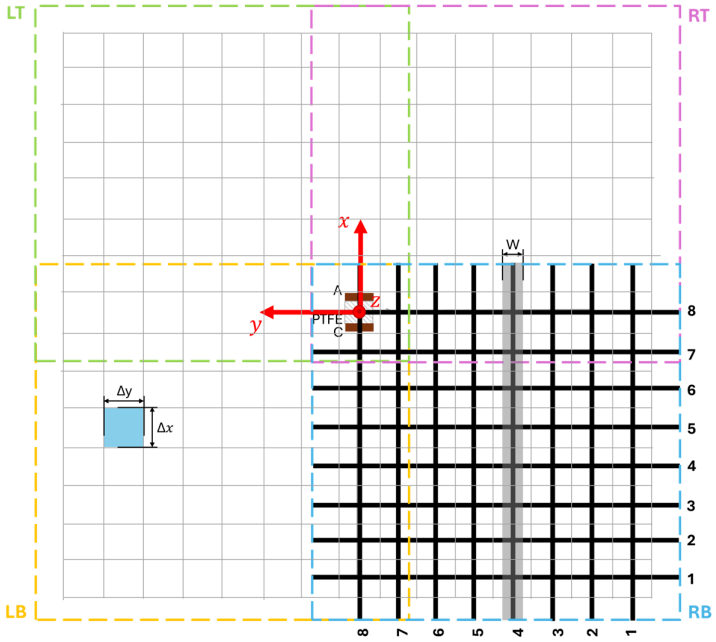

(b) Cartesian grid used for the reconstruction of the exhaust cross section with uniform cell size given by Δx, Δy, and subgrids covered by each of the four overlapping probe array positionings (color dashed lines). Horizontal and vertical probe locations are shown for the RB positioning (thick lines). Each wire probe spans various grid cells. The sheath width W is sketched for one of the probes. Note that the z axis points toward the reader.

Figure 3: **Sketch of the experimental setup.**

First, we discretize the cross section of the plume into a uniform Cartesian grid, as shown in figure 3(b), with grid spacing Δx, Δy. Mind that the x axis here points along the vertical direction. The model of $j(x, y, t)$ to be obtained is piece-wise constant over each cell of this grid, for each instant of time.

For each positioning of the probe array in the experiment, there are N_h horizontal probes parallel to the y axis, at fixed x_i positions ($i = 1, \ldots, N_h$), and N_v vertical wire probes parallel to the x axis at fixed y_j positions ($j = 1, \ldots, N_v$). Each horizontal (respectively, vertical) probe has a total measurement length of $L_y = N_v \Delta y$ ($L_x = N_h \Delta x$), and falls along the centerline of a definite row (column) of the Cartesian grid, spanning entirely a total of N_v (N_h) cells. Therefore, for each positioning, the probes of the array span a subgrid of the Cartesian grid fully. [In actuality, the probes do not span fully the last cell, missing 25% of it. Also, they protrude a bit outside of the grid edges. These two aspects are neglected in the current version of the algorithm for simplicity, at the cost of a small error in our reconstruction.]

The probes collect ion current over a rectangular area defined by their length L_y (L_x), and an effective collection width, W, that includes the wire diameter and the (estimated) sheath thickness, and which is assumed to be always smaller than Δx, Δy. We may formally write the probe collected ion currents V_i and H_j as

$$\begin{aligned} H_i(t) &= \int_{L_y} \mathrm{d}y \int_{x=x_i-W/2}^{x=x_i+W/2} j(x, y, t)\mathrm{d}x, & i &= 1, \ldots, N_h; \\ V_j(t) &= \int_{L_x} \mathrm{d}x \int_{y=y_j-W/2}^{y=y_j+W/2} j(x, y, t)\mathrm{d}y, & j &= 1, \ldots, N_v. \end{aligned} \tag{1}$$

Next, we model the current density map $j(x, y, t)$ collected as the product of a magnitude $J(t)$ and two normalized, spatially piece-wise uniform functions $f(x, t)$ and $g(y, t)$, all of them to be determined,

$$j(x, y, t) = J(t) f(x, t) g(y, t). \tag{2}$$

The dimensionless function f (g) has spatially constant values $f_i(t)$ ($g_j(t)$) over each row (column) of the subgrid spanned by the probes. Furthermore, they satisfy the following normalization constraints at each instant of time:

$$\sum_i f_i \Delta x = L_x; \qquad \sum_j g_j \Delta y = L_y. \tag{3}$$

Applying this functional decomposition to the integrals in equation 1 yields the approximations

$$\begin{aligned} \tilde{H}_i(t) &= J(t) f_i(t) \sum_j g_j(t) W \Delta y = J(t) f_i(t) W L_y, & i &= 1, \ldots, N_h; \\ \tilde{V}_j(t) &= J(t) g_j(t) \sum_i f_i(t) W \Delta x = J(t) g_j(t) W L_x, & j &= 1, \ldots, N_v. \end{aligned} \tag{4}$$

Equating

$$H_i(t) = \tilde{H}_i(t), \qquad V_j(t) = \tilde{V}_j(t), \tag{5}$$

and considering the normalization constraints 3, yields a set of $N_v + N_h + 2$ equations for the $N_v + N_h + 1$ unknowns $f_{si}(t)$, $g_{sj}(t)$, and $J(t)$ at each positioning and for each instant of time. This set of equations is generally incompatible, as can be easily seen by considering the following sums, which would both determine $J(t)$:

$$\sum_i H_i = \sum_i \tilde{H}_i \equiv J(t) L_x L_y \frac{W}{\Delta x} \qquad \sum_j V_j = \sum_j \tilde{V}_j \equiv J(t) L_x L_y \frac{W}{\Delta y} \tag{6}$$

To resolve this issue, equations (6) are solved for $J(t)$ using least-squares, yielding

$$J(t) = \frac{1}{L_x L_y W} \sqrt{\left(\sum_i H_i \Delta x\right)^2 + \left(\sum_j V_j \Delta y\right)^2}. \tag{7}$$

Then, once $J(t)$ has been so determined, equations (5) directly yields the the unknowns f_i, g_j.

Finally, when some of the cells of the Cartesian grid are spanned by two or more overlapping probe array positionings, as in the current work, the mean of the multiple solutions is taken on those cells. This overlap can be regarded as a means to further improve the statistical significance of the solution in that region; in addition, the standard error among the solutions provides a useful measure of the error in the model.

IV. Results

A. Electrical response of the discharge and propellant consumption

The anode voltage response $V(t)$ at the nominal point (1000 V of discharge voltage V_0 and 6 μF of capacitance C) is shown in Figure 4 averaged along multiple shots; the shaded area represents the standard deviation. The signal exhibits damped oscillations with natural frequency, $\omega \sim 100$ kHz, and with the signal amplitude decaying by a factor of 10 after about 5 μs. Good repeatability among pulses is observed, especially along the first cycle of the discharge. The current setup with the new capacitors exhibits a similar discharge time than the one used in our previous work,[19] albeit with a slightly lower frequency. The estimated resistance (R) and inductance (L) values from fitting an RLC circuit with constant parameters to the first cycles of the discharge are around 40 mΩ and 40 nH respectively.

High-frequency noise in the order of magnitude of $O(10)$ MHz on $V(t)$ is noticeable around the breakdown instant, and often at the signal minima/maxima. The later could be related to late reignitions that may occur upon voltage inversion.[9,15–18]

After averaging over 4028 firings, we find that the ablated mass per firing falls within 3.9 ± 0.2 μg at the nominal operational point.

No charring accumulated on the PTFE surface along 10^4 firings. No clear contamination patterns around it were neither found to robustly suggest plume deviation.

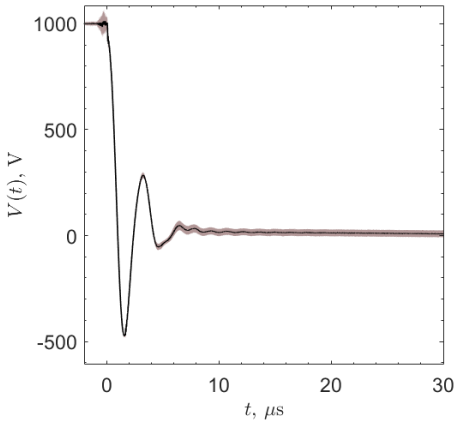

Figure 4: **Time signal of the anode voltage $V(t)$ averaged over multiple firings, and its standard deviation (shaded area).**

B. Plume cross section characterization

Figure 5 displays the time response of the measured ion saturation current along horizontal probes at $x = 0$ and along vertical probes at $y = 0$. These locations correspond to the probe overlap existing among the different frame positionings, i.e., each one of them is covered by two positionings. Therefore, figure 5 not only provides valuable information about the central "crosshair" in the measurement plane, but additionally, serves to partially validate that the positioning error of the probe system is rather small.

Overall, probes begin collecting current at around 2 μs after the discharge breakdown, which is set as $t = 0$ for any shot, and the signal has essentially vanished 15 μs afterward. It can be seen that the shot-to-shot ion current repeatability of the measured current signals is worse than that of the discharge voltage $V(t)$ shown in figure 4.

In general, along the four locations shown in figure 5, the average response over the shots reveals that mainly three bumps are clearly visible. These take place at around $t_1 = 3.38$ μs, $t_2 = 5.34$ μs and $t_3 = 7.64$ μs respectively. These peaks are hypothesized to correspond to distinct ion groups, likely of different charge/mass ratios, as was earlier indicated in our previous work.[19] In that work, the mean speed of each ion group was 50, 32 and 18 km/s, correspondingly. In figure 5, out of the three bumps, the second one typically drives the largest current; note, however, that in $V_{B8}(t)$, where the first peak reaches comparable or even higher maximal instantaneous values than the second.

It is also evident that H_{R8} collects more current than the other three, followed by V_{B8}. This already suggests some asymmetry is present in the exhaust, whose maximum current seems to be partially deviated toward the RB sector. This is further confirmed below.

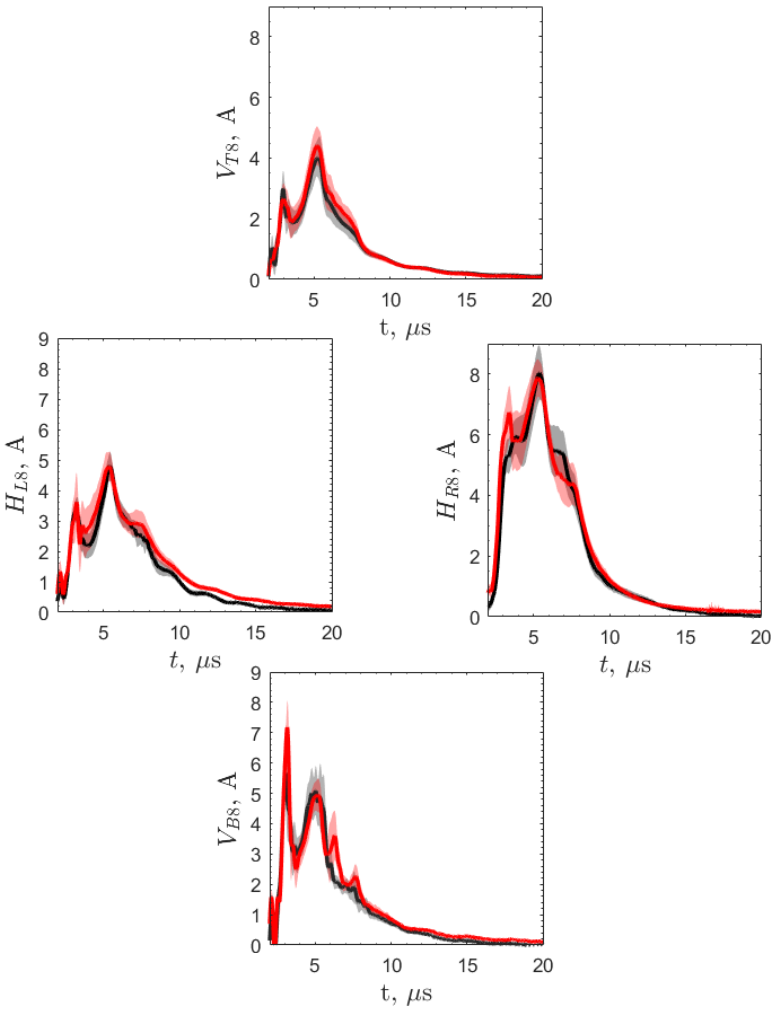

Figure 5: **Horizontal and vertical ion saturation current measurements averaged over multiple firings (solid lines) and their standard deviation (shaded area) at overlapping locations on the central crosshair of the exhaust (see figure 3(b))**. Each subplot displays the current measured at a given location, accessed from two different positionings of the probe array. Horizontal measurements $H_{R8}(t)$ and $H_{L8}(t)$ show in black, measurements taken from the positionings right-top RT $(-y, +x)$ and left-top LT $(+y, +x)$ respectively, and in red for the bottom positionings RB $(-y, -x)$ and LB $(+y, +x)$. For vertical measurements $V_{B8}(t)$ and $V_{T8}(t)$, black lines refer to the RB and RT positionings, and red ones for the LB and LT.

The time-series measurements for some selected horizontal and vertical probes in positioning RB are presented in figure 6(a),(b) respectively. We find that this positioning indeed shows higher current values

than the other three positionings. Overall magnitude for horizontal measurements H_{RBi} is larger at $x = -2$ and 0 cm, which features a near-identical response, except for the first maxima, which is around 8 A for $x = -2$ cm and 6 A for $x = 0$ cm. These two probes exhibit three distinct bumps, and therefore measure the same behavior as in figure 5. In contrast, probes at $x = -6$ and $x = -10$ cm gather a smaller current with a flatter time response. This could indicate that the contributions of the different ion groups mix on the exhaust periphery. A small delay exist in the initial rise time of these two curves, compared with those at $x = 0, -2$ cm.

The vertical measurements show the largest currents at $y = -2$ and $y = -6$ cm. Once again, two distinct behaviors are found, for the probes closer and farther away to the exhaust center. At locations $y = 0, -2$ cm, two ion groups are identifiable. The contribution of the third one, while less evident than in the central horizontal measurements, presumably contributes to the slow decay of the signals after $t = 6$ μs. The probes at $y = -6, -10$ cm, on the other hand, show a broad flat-peaked current curve, suggesting again that the contributions of the different ion groups are tangled at these locations. Additionally, the current at $y = -10$ cm seems to arrive at a later time than at $y = -6$ cm.

Indeed, it is generally observed that, whatever the frame positioning, at distances $|x|$ or $|y|$ larger than the maximum-current probe location within the positioning, the farther a probe is from the thruster, the later it starts collecting current.

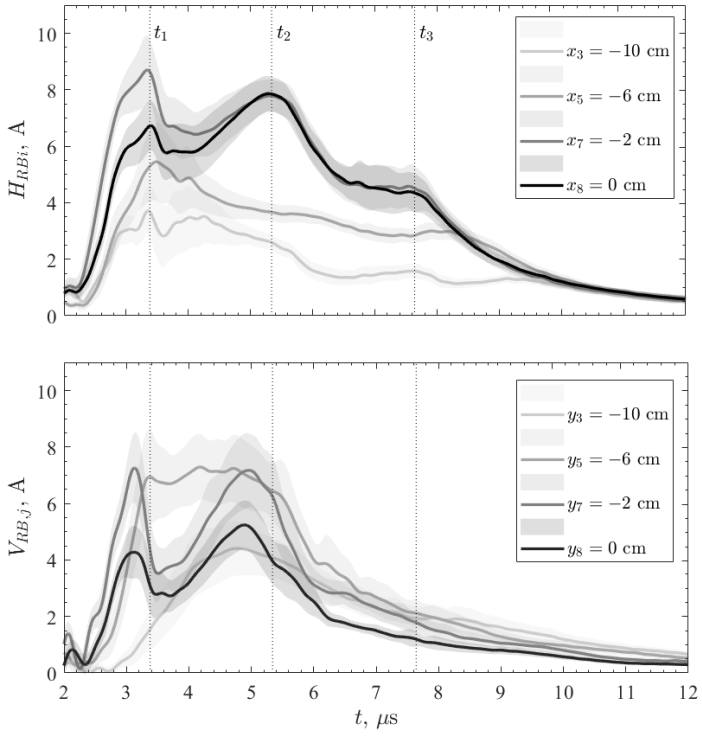

Figure 6: **Ion saturation current measurements of some horizontal $H_{RBi}(t)$ and vertical $V_{RBj}(t)$ probes along the right-bottom RB positioning $(-x, -y)$ of the plume section** (setup in figure 3(b)), averaged along multiple firings (solid lines) and their standard deviation (shaded areas). t_1, t_2, t_3 indicate the peak-current times along $H_{RB8}(t)$, $x = 0$ cm, serving as reference times for further discussions.

Figure 7 presents at the three different times of interest t_1,t_2,t_3, the reconstructed 2D current density distribution $j(x, y)$ in the Cartesian grid of the plume cross section, together with the row-wise and column-wise integrals. The total current in the grid at each instant, I_T, is reported as well, integrating over the cells.

Results concerning the center of the j distribution reveal certain displacement of the exhaust towards the RB sector. At t_1 (panel (a)), the center of the distribution is located at $(c_{j_x}, c_{j_y}) = (-2.2, -1.1)$ cm, slightly moving over time towards the center of the reference system (panel (b)), with this shift being particularly

noticeable at t_3 (panel (c)), with $(c_{j_x}, c_{j_y}) = (-0.6, -0.6)$.

At t_1, panel (a), $j(x, y)$ decreases with $|x|$, with a stronger decaying rate for $+x$ than for $-x$. In contrast, the behaviour of $j(x, y)$ with y exhibits a higher dispersion and reveals two bumps at $+y$ and $-y$ respectively, with the $-y$ one driving more current. As plasma expands, these bumps move apart and gradually flatten. At late times, a more uniform distribution along the entire cross section applies, as it is shown in t_3 in panel (c_j). At that time, the $j(x, y)$ center mostly aligns with the center of the reference system but still in RB.

Plasma spreading more along the plane parallel to the electrodes than to the perpendicular one to it has been also reported in the literature[23,39] for parallel plate APPT configurations.

The reconstructed total current in the Cartesian grid, $\tilde{I}_{tot}$, peaks about 250 A. Most of the current reaches the probe array at $t = 5$–6 μs, which according to our previous work,[19] corresponds to ions with an average velocity of 32 km/s, thermal spread around 10 km/s, and originated at the primary ignition.

The time-integral charge density distribution $\rho = \int j(x, y)\mathrm{d}t$, computed for the whole ion collection time (2 –15 μs) is presented in figure 8. The $\rho(x, y)$ distribution is driven mainly by the first instants of the discharge, when the current density is large, and confirms our previous conclusions on the shape of the exhaust: that is, ions distribute differently along x (i.e. the direction of the applied electric field across the electrodes), where they show a single peak, and along y (i.e., the direction of the plasma-induced magnetic field) where they show two peaks, one at each side of the centerline, with the $-y$ one weighing more. The accumulated collected ions are slightly concentrated towards the RB sector, with the center of the distribution located at $(c_{\rho_x}, c_{\rho_y}) = (-1.4, -0.6)$. Maximum ρ falls under 25 mCm^{-2}.

V. Conclusion

The time-resolved expansion of the exhaust of a small ablative pulsed plasma thruster prototype has been experimentally characterized by means of a novel diagnostic system consisting of a Langmuir probe grid working in the ion saturation regime. These probes measure the line integral of the current distribution on a plume cross section. A simple algorithm to resolve the inverse reconstruction problem by variable separation is proposed. This work is aims to complement our time-of-flight characterization of the exhaust axis,[19] by providing time- and space-resolved data on the shape of the expansion away from that centerline. Beyond their relevance on the characterization of the time-dependent exhaust divergence angle, the thruster performance and their interest for spacecraft/plume interaction analyses, these results constitute an additional step towards a clearer understanding of the discharge physics in PPTs.

The data have allowed to assess the instantaneous divergence of the plasma jet and its evolution in time, as well as the existence of asymmetries, multiple peaks, and distinct distributions along the x and y directions: the current density map is slightly concentrated towards the cathode side of the section, and one of the channel lateral sides. Plasma spreads less along the cathode-to-anode direction (i.e., aligned with the applied electric field or x axis), which seems to be characteristic in parallel plate configurations.[23,39] A single-peaked profile along the x axis is seen, while two peaks characterize the distribution along the parallel direction to the self-induced magnetic field (y), at each one of the sides of the channel, respectively. The current density distribution becomes more uniform at later times. These conclusions are also observable on the cumulative charge density distribution.

Time-wise, three bumps are observed in the ion current, consistent with the existence of different ion groups identified in our previous work.[19] The second group arriving at the probes drives the major part of the plume current. On individual wire probes, these ion groups are only easily identifiable near the central positions of the exhaust. For probes near the periphery of the cross section, the contributions of the three ion groups become mixed. This is explained, in part, by the variation of the time of arrival of each ion group along the length of the probe, which, in general, can be comparable to the time between ion groups at probe locations $\geq |8|$ cm from the central line. Nevertheless, cross-section reconstruction shows that the three ion groups are present and indeed govern the measured current everywhere.

The new diagnostic method can be refined in several ways. First, a larger cross sectional area of the exhaust can be covered by either increasing the number of frame positionings or developing a larger frame (currently constrained by the dimensions of the openings of the vacuum chamber used). A major improvement of the reconstruction method would be to model the sheath width, which defines the effective collection width of the probes (here taken as constant and uniform). This, however, requires time- and space-resolved data on the electron density, which is currently unavailable. Also, other models (e.g. piece-wise linear) are viable extensions for the reconstruction, and may be explored in the future.

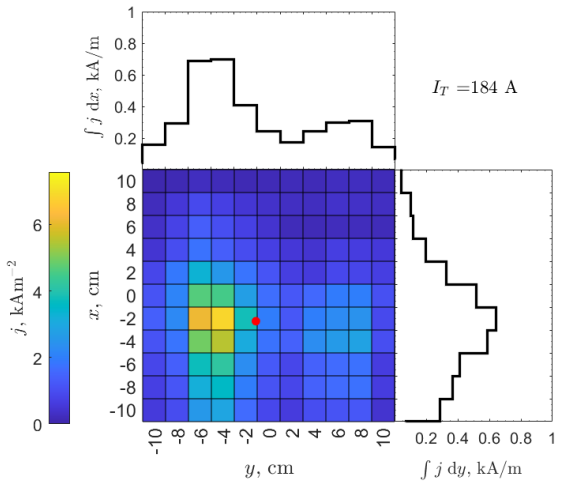

(a) $t_1 = 3.38$ μs. $(c_{j_x}, c_{j_y}) = (-2.2, -1.1)$ cm.

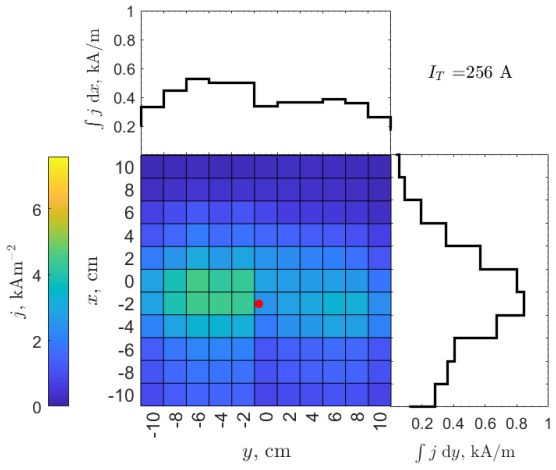

(b) $t_2 = 5.34$ μs. $(c_{j_x}, c_{j_y}) = (-2.0, -0.6)$ cm.

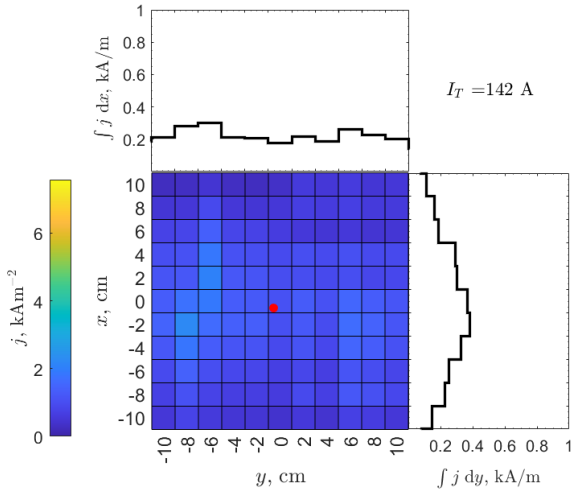

(c) $t_3 = 7.69$ μs. $(c_{j_x}, c_{j_y}) = (-0.6, -0.6)$ cm.

Figure 7: **Current density distribution map $j(x, y)$, its integrals alongx, y, and the total current through the plume cross section I_T, at the three times of interest t_1, t_2, t_3, corresponding to those identified in figure 6. The red dot locates the center of the $j(z, y)$ distribution.**

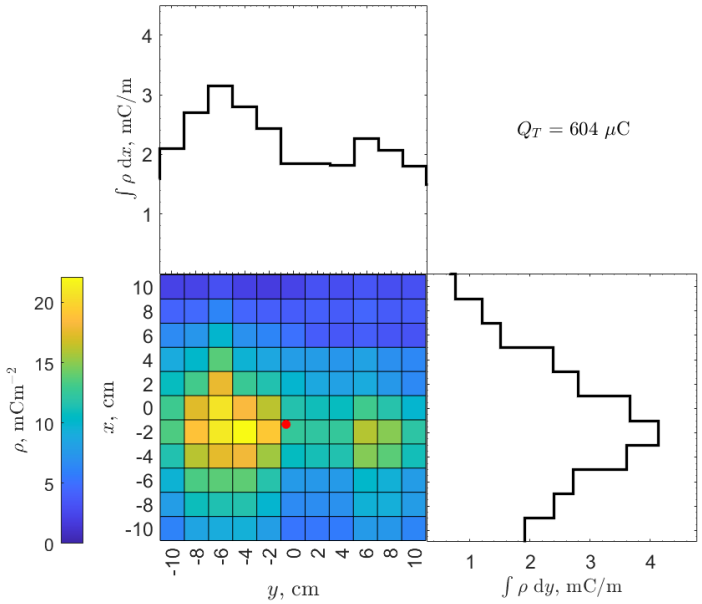

Figure 8: **Time-integrated charge density distribution map $\rho(x, y)$ and its integrated profiles along x,y.** The red dot indicates the center of the $\rho(x, y)$ distribution, at $(c_{\rho_x}, c_{\rho_y}) = (-1.4, -0.6)$ cm. The total charge integrated over the cross sectional area, Q_T, is also given. 2.

Acknowledgments

This work was been supported by the MARTINLARA project, funded by the Comunidad de Madrid, under Grant reference P2018/NMT-4333 MARTINLARA-CM.

Additional support came from the ESPEOS project, funded by the Agencia Estatal de Investigación (Spanish National Research Agency), under Grant number PID2019-108034RB-I00/AEI/10.13039/501100011033.

References

[1]Burton, R. and Turchi, P., "Pulsed plasma thruster," Journal Propulsion and Power, Vol. 14, 1998, pp. 716–735.

[2]Solbes, A., Thomassen, K., and Vondra, R., "Analysis of solid teflon pulsed plasma thruster," Journal of Spacecraft and Rockets, Vol. 7, No. 12, 1970, pp. 1402–1406.

[3]Rayburn, C. D., Campbell, M. E., and Mattick, A. T., "Pulsed Plasma Thruster System for Microsatellites," Journal of Spacecraft and rockets, Vol. 1, No. 42, 2005.

[4]Miller, H. C., "Surface flashover of insulators," IEEE Transactions on Electrical Insulation, Vol. 24, No. 5, 1989, pp. 765–786.

[5]Brady, M. E. and Aston, G., "Pulsed plasma thruster ignitor plug ignition characteristics," Journal of Spacecraft and Rockets, Vol. 20, No. 5, 1983, pp. 450–451.

[6]Bogatyi, A. V., D'yakonov, G. A., and Semenikhin, S., "Mechanisms for the Formation of Parasitic Propellant Consumption in an Ablative Pulsed Plasma Thruster," Cosmic Research, Vol. 57, 2019, pp. 310 – 316.

[7]Molina-Cabrera, P., Herdrich, G., Fausolas, S., Schoenherr, T., and Komurasaki, K., "Pulsed Plasma Thrusters: a worldwide review and long yearned classification," 2011.

[8]Levchenko, I., Bazaka, K., Ding, Y., Raitses, Y., Mazouffre, S., Henning, T., Klar, P. J., Shinohara, S., Schein, J., Garrigues, L., Kim, M., Lev, D., Taccogna, F., Boswell, R. W., Charles, C., Koizumi, H., Shen, Y., Scharlemann, C., Keidar, M., and Xu, S., "Space micropropulsion systems for Cubesats and small satellites: From proximate targets to furthermost frontiers," Applied Physics Reviews, Vol. 5, No. 1, 02 2018, pp. 011104.

[9]Jahn, R., Physics of Electric Propulsion, Dover, 2006.

[10]Keidar, M., Boyd, I. D., and Beilis, I. I., "Ionization and ablation phenomena in an ablative plasma accelerator," Journal of Applied Physics, Vol. 96, 2004, pp. 5420–5428.

[11]Mikellides, P. and Turchi, P., Modeling of late-time ablation in Teflon pulsed plasma thrusters.

[12]Popov, G. A., Orlov, M., Antropov, N. N., Gomilka, L. A., D'Iakonov, G. I., and Krivonosov, I. I., "Parameters of plasmoids injected by PPT," 1997.

[13]Thomassen, K. I. and Vondra, R. J., "Exhaust velocity studies of a solid Teflon pulsed plasma thruster," Journal of Spacecraft and Rockets, Vol. 9, No. 1, 1972, pp. 61–64.

[14]Peradzyński, Z., Makowski, K., and Kurzyna, J., "Early stage of the discharge in ablative pulsed plasma thrusters," Plasma Sources Science and Technology, Vol. 28, No. 2, feb 2019, pp. 024001.

[15]Koizumi, H., Noji, R., Komurasaki, K., and Arakawa, Y., "Plasma acceleration processes in an ablative pulsed plasma thruster," Physics of Plasmas, Vol. 14, No. 3, 2007.

[16]Kumagai, N., Igarashi, M., Sato, K., Tamura, K., Kawahara, K., and Takegahara, H., "Plume Diagnostics in Pulsed Plasma Thruster," 2002.

[17]Lau, M., Manna, S., Herdrich, G., Schönherr, T., and Komurasaki, K., "Investigation of the plasma current density of a pulsed plasma thruster," Journal of Propulsion and Power, Vol. 30, No. 6, 2014, pp. 1459–1470.

[18]Loebner, K. T. K., Underwood, T. C., and Cappelli, M. A., "Evidence of Branching Phenomena in Current-Driven Ionization Waves," Phys. Rev. Lett., Vol. 115, Oct 2015, pp. 175001.

[19]Barquero, S., Navarro-Cavallé, J., and Merino, M., "Pulsed plasma thruster exhaust reconstruction," Plasma Sources Science and Technology, Vol. 33, No. 4, apr 2024, pp. 045007.

[20]Spanjers, G. G., Lotspeich, J. S., McFall, K. A., and Spores, R. A., "Propellant Losses Because of Particulate Emission in a Pulsed Plasma Thruster," Journal of Propulsion and Power, Vol. 14,No 4, 1998, pp. 554–559.

[21]Keidar, M., Boyd, I. D., and Beilis, I. I., "Model of Particulate Interaction with Plasma in a Teflon Pulsed Plasma Thruster," Journal of Propulsion and Power, Vol. 17, No. 1, 2001, pp. 125–131.

[22]Sch´onherr, T., Nees, F., Arakawa, Y., Komurasaki, K., and Herdrich, G., "Characteristics of plasma properties in an ablative pulsed plasma thruster," Physics of Plasma, Vol. 20, No. 3, 2013, pp. 033503.

[23]Myers, R., Arrington, L., Pencil, E., Carter, J., Heminger, J., and Gatsonis, N., "Pulsed plasma thruster contamination," 32nd joint propulsion conference and exhibit, 1996, p. 2729.

[24]Markusic, T. and Spores, R., Spectroscopic emission measurements of a pulsed plasma thruster plume.

[25]Eckman, R., Pulsed plasma thruster plume diagnostics.

[26]Parker, K., "Pulsed Plasma Thruster plume analysis," Acta Astronautica, Vol. 53, No. 4, 2003, pp. 789–795, The New Face of Space Selected Proceedings of the 53rd International Astronautical Federation Congress.

[27]Hoskins, W. A., Rayburn, C., and Sarmiento, C. J., "Pulsed Plasma Thruster Electromagnetic Compatibility: History, Theory, and the Flight Validation on E0-1," AIAA/ASME/SAE/ASEE Joint Propulsion Conference and Exhibit, 2003.

[28]Gatsonis, N. A., Byrne, L. T., Zwahlen, J. C., Pencil, E. J., and Kamhawi, H., "Current-mode triple and quadruple Langmuir probe methods with applications to flowing pulsed plasmas," IEEE transactions on plasma science, Vol. 32, No. 5, 2004, pp. 2118–2129.

[29]Keidar, M., Boyd, I. D., Antonsen, E. L., Gulczinski, F. S., and Spanjers, G. G., "Propellant Charring in Pulsed Plasma Thrusters," Journal of Propulsion and Power, Vol. 20, No. 6, 2004, pp. 978–984.

[30]Edamitsu, T. and Tahara, H., "Experimental and numerical study of an electrothermal pulsed plasma thruster for small satellites," Vacuum, Vol. 80, No. 11-12, 2006, pp. 1223–1228.

[31]Shaw, P., Lappas, V., and Underwood, C., "Design, development and evaluation of an 8 μPPT propulsion module for a 3U CubeSat application," International Electric Propulsion Conference.

[32]Guarducci, F., Coletti, M., and Gabriel, S., "Design and testing of a micro pulsed plasma thruster for Cubesat application," International Electric Propulsion Conference, 2011, pp. 2011–239.

[33]Schönherr, T., Komurasaki, K., and Herdrich, G., "Propellant Utilization Efficiency in a Pulsed Plasma Thruster," Journal of Propulsion and Power, Vol. 29, No. 6, 2013, pp. 1478–1487.

[34]Wang, W., Liu, F., Wang, X., and Liang, R., "Study on electron temperature in an ablative pulsed plasma thruster by optical emission spectroscopy," Europhysics Letters, Vol. 101, No. 5, mar 2013, pp. 55001.

[35]Coletti, M., Ciaralli, S., and Gabriel, S. B., "PPT development for nanosatellite applications: experimental results," IEEE Transactions on Plasma Science, Vol. 43, No. 1, 2015, pp. 218–225.

[36]Pellegrini, G., Mancini, E., Paganucci, F., and Andrenucci, M., "Development and Characterization of a Pulsed Plasma Thruster," Space Propulsion 2018, 2018.

[37]RUDOLPH, L. and JONES, R., Pulsed plasma thruster contamination studies.

[38]Vondra, R., Thomassen, K., and Solbes, A., "A pulsed electric thruster for satellite control," Proceedings of the IEEE, Vol. 59, No. 2, 1971, pp. 271–277.

[39]Jakubczak, M., Jardin, A., and Kurzyna, J., "Analysis of composition and dynamics of the plasma plume emitted by a 1 J pulsed plasma thruster fed with polytetrafluoroethylene and determination of thruster efficiency components," Physics of Plasmas, Vol. 31, No. 5, 05 2024, pp. 053501.

[40]Barquero, S., Merino, M., and Navarro-Cavallé, J., "Experimental plume characterization of a low-power Ablative Pulsed Plasma Thruster (APPT)," 37^{th} International Electric Propulsion Conference, No. IEPC-2022-556, Electric Rocket Propulsion Society, Boston, MA, June 19-23, 2022.